



## Simulation of Film Boiling Heat Transfer in Complex Geometries using Front Tracking Method

A. Sedaghatkish and S. Mortazavi<sup>†</sup>

*Department of Mechanical Engineering, Isfahan University of Technology, Isfahan, 8415683111, Iran*

<sup>†</sup>Corresponding Author Email: [saeedm@cc.iut.ac.ir](mailto:saeedm@cc.iut.ac.ir)

(Received May 20, 2018; accepted September 17, 2018)

### ABSTRACT

Film boiling has various industrial applications especially in heat exchangers. Studying this phenomenon on complex geometries and investigating heat transfer coefficient is desired by many industries. The numerical method used here is a finite difference/front tracking method which is developed independently for film boiling in complex geometries. The film boiling over one, two or more cylinders is simulated using this method. The effect of dimensionless parameters namely Grashof and Jacob numbers are investigated for one cylinder. The effects of spacing, angle, and diameter are investigated for two cylinders. For the case with many cylinders, the effects of different geometrical configurations (regular and staggered) and number of rows are investigated by calculating the average Nusselt number on each cylinder. It is observed that the cylinder spacing does not have any significant effect on the Nusselt number for the upper cylinder. However the angle and cylinder diameter significantly affect the Nusselt number for the upper cylinder. In regular configuration, the Nusselt numbers for the upper cylinders are relatively uniform and higher than lower cylinders. In the staggered configuration, however, the Nusselt numbers of the upper cylinders are different, non-uniform, and higher than those of the regular arrangement.

**Keywords:** Film boiling; Front tracking method; Complex geometries; Heat transfer.

### NOMENCLATURE

A	area	S	tangential vector
c	heat capacity	T	temperature
dt	time step	u	velocity
dx	mesh size		
F	surface tension force	$\theta$	angle
g	gravity	$\kappa$	curve function
Gr	Grashof number	$\rho$	density
h	heat transfer coefficient, latent heat	$\bar{D}$	dimensionless diameter
H	Indicator function	$\mu$	dynamic viscosity
Ja	Jacob number	$\nu$	kinetic viscosity
k	thermal conduction coefficient	$\tau$	shear stress
L	reference length	$\sigma$	surface tension coefficient
n	normal vector	$\alpha$	thermal diffusion coefficient
Nu	Nusselt number	$\delta$	vapor layer thickness
P	pressure	$\lambda$	wave length
Pr	Prandtl number		
q	heat flux		
R	radius		

### 1. INTRODUCTION

So far, many developments have been performed to improve heat transfer in chemical and oil industries as well as power plants. Researchers are still trying

to maximize the heat transfer coefficient. This results in enhanced efficiency, reduced energy consumption, lower demand for construction materials, lower cost of fuel and optimization of the space required for constructing heat exchangers.

In natural convection, single phase fluid flow occurs at a heat transfer coefficient in the range 5-10  $\text{W/m}^2\text{K}$  and 100-200  $\text{W/m}^2\text{K}$  for gases and liquids, respectively. In forced convection, the coefficient reaches 30-150  $\text{W/m}^2\text{K}$  and 100-1000  $\text{W/m}^2\text{K}$  for gases and liquids, respectively. For multiphase flows (e.g. boiling and condensation), however, heat transfer coefficient may reach as high as 4000-5000  $\text{W/m}^2\text{K}$ . Such a high heat transfer coefficient during boiling process may resolve difficulties with respect to the heat transfer coefficient for designers of heat exchangers (Swain and Kumar, 2014).

So far, many researchers have undertaken numerous experiments to investigate pool boiling process. Based on the results of these experiments, which were performed in scales similar to real heat exchangers, one can enhance heat transfer in a heat exchanger. In two-phase shell and tube heat exchangers, pool boiling occurs on the shell side where it is easier to exhaust generated vapor bubbles. Therefore, the hot fluid flows inside the tubes where its temperature decreases along the heat exchanger. The cold fluid boils on the shell side, and usually has a lower boiling point. Numerous parameters affect the heat transfer coefficient in pool boiling. A brief review on related research works and the affecting parameters are presented in the following sections.

Kang (2005) investigated pool boiling outside and inside a tube with a diameter 51 mm. He performed experiments at atmospheric pressure, and used water as the boiling fluid. Outside the tube, maximum and minimum heat transfer coefficients were observed at polar angle  $\theta = 45^\circ$  and  $\theta = 180^\circ$ , respectively. The main boiling mechanism outside the tube was the liquid disruption, and rise as well as coalescence of bubbles that enhanced heat transfer coefficient; the higher the heat flux of the tube, the higher would be this effect. The heat transfer coefficient increases with  $\theta$  up to  $45^\circ$ , and decreases with  $\theta$  up to  $180^\circ$ .

Liu and Qiu (2002a) investigated the fluid type, surface type, and pipe spacing in a set of pipes. They further considered the effect of using numerous pipes rather than a single pipe, and found enhanced heat transfer coefficient with larger number of tubes.

The rolled-surface pipes had the best heat transfer coefficients compared to other surfaces (including smooth surface) at medium fluxes. This was due to the fact that the rolled surface has a large number of small holes when they contribute to the formation of nucleation sites in nucleate boiling. The effect of fluid type on heat transfer coefficient was also considered in this investigation. They concluded that salt concentration does not have a significant effect on convective heat transfer coefficient. They performed a comparison on heat transfer coefficient for a set of rolled pipes with smooth surface, and single rolled pipes with smooth surface. They concluded that, at heat fluxes below  $100 \text{ kW/m}^2$ , the heat transfer coefficient for the set of rolled pipes is higher than that of a single pipe.

In another investigation performed by Liu and Qiu (2002b), the effects of pipe spacing, working pressure of experiment, and also position or arrangement of the pipes were studied. Moreover, investigations have shown that there is an optimum spacing wherein the heat transfer coefficient is maximum. They found that, whenever the surface-to-surface pipe spacing is equal to or greater than 0.3 mm, and the heat transfer is in nucleate boiling regime, the heat transfer coefficient decreases with increasing the spacing.

They investigated the effect of pipe spacing, and concluded that when the spacing is 0.3 mm, pipe arrangement has no effect on heat transfer coefficient. But if the pipe spacing is set to 1 mm, the value of heat transfer coefficient on the upper pipe will be higher than that on the lower one. This is due to the rise and collision of bubbles from lower pipes to the upper pipes. The higher the distance between lower and upper pipes, the larger will be the fluid disturbance resulted from dynamic collision of the lower bubbles. As a result heat transfer coefficient enhances.

Moreover, the effect of test pressure on heat transfer coefficient was evaluated. They (Liu and Qiu) showed that, when the pipe spacing is 0.3 mm, a change in pressure does not significantly affect the heat transfer coefficient. However, if the pipe spacing is set to 1 mm, it is observed that an increase in pressure will enhance heat transfer coefficient.

In an experimental study, Hahne *et al.* (1983) considered the effect of finned pipes on heat transfer coefficient. In addition, they used two pipes instead of one pipe. They found that, the heat flux at the lower pipe tends to affect heat transfer coefficient of the upper pipe. This phenomenon is due to the rise of bubbles from the lower pipe which disturb the flow around the upper pipe.

In another investigation, Saini and Varma (1995) studied the effect of velocity and flow rate on the pipes in the boiling process, and found that the higher the flow rate on the pipes, the higher will be the heat transfer coefficient.

One of the most recent works performed in this respect, is that by Kang (2015a). In his experiments, he investigated the effect of two pipes and heat flux of every pipe on heat transfer coefficient. The evident effect of the two pipes in heat transfer coefficient is visible when heat flux of the lower pipe exceeds that of the upper one, and heat flux of the upper pipe being below  $60 \text{ kW/m}^2$ . The bubbles risen from the surface of the pipes were imaged at different flow conditions. When heat fluxes are low, larger bubbles are observed on the upper pipe. They found that the higher the heat fluxes, the larger will be the size of bubbles.

In another experimental investigation by Kang (2015b), the effect of the angle between the pipes was investigated. In this experimental work, it was observed that the heat transfer coefficient of the upper pipe is higher if the angle between two cylinders is close to  $90^\circ$ . In other words, the heat

transfer coefficient will be maximum if the upper pipe is below the lower pipe along the vertical direction. Of course, this result is valid as long as the heat flux of the upper pipe is lower than that of the lower pipe. In such case, the bubbles produced from the lower pipe could well affect the upper pipe.

To the best of our knowledge, in all of the works reported so far, water has been the fluid when boiling was studied. All experiments performed at a pressure of 1 bar or ambient pressure. Another group of works are semi-experimental works. In these studies, analytical relationships are used along with experimental data in order to extract some correlations for Nusselt number in terms of the dimensionless numbers such as Grashof, Jacob, and Prandtl. In fact, using these dimensionless parameters, the heat transfer rate is solely related to the fluid properties and the flow behavior addressed by these dimensionless numbers. They obtained correlations for the heat transfer coefficient based on curve fitting of the experimental data. Some examples of such correlations in film boiling over cylinder and flat surfaces are considered.

Berenson (1961) was among those who investigated film boiling by assuming hydrodynamic instability and sequential release of bubbles while taking into account bubbles spacing. Considering the largest instability wavelength in film boiling over flat surface, he calculated Nusselt number on the flat surface as follows:

$$Nu = 0.425 \left( \frac{Gr Pr}{Ja} \right)^{0.25} \quad (1)$$

This relationship is valid for laminar flow at a heat flux close to the minimum flux required for film boiling regime. Klimenko (1961) obtained a relationship for both laminar and turbulent flow regimes. He estimated the Nusselt number in the vicinity of a flat surface via the following relationship which includes 20% relative error with respect to experimental data.

For laminar flow:

$$Nu = c Gr^n Pr^m f_k \quad (2)$$

$$c = 0.19 \quad n = \frac{1}{3} \quad m = \frac{1}{3} \quad f_k = f_l \quad (3)$$

$$f_l = \begin{cases} 0.89 Ja^{-\frac{1}{3}} & , Ja < 0.71 \\ 1 & , Ja \geq 0.71 \end{cases} \quad (4)$$

and for turbulent flow:

$$c = 0.0216 \quad n = \frac{1}{2} \quad m = \frac{1}{3} \quad f_k = f_t$$

$$f_t = \begin{cases} 0.71 Ja^{\frac{-1}{2}} & , Ja < 0.5 \\ 1 & , Ja \geq 0.5 \end{cases} \quad (5)$$

For film boiling over the surface of a cylinder, Broomley (1950), Breen and Westwater (1962), and Sakurai and Shiotsu (1990 a,b) obtained the following relationships for Nusselt number on the surface of a cylinder in terms of the dimensionless parameters. These are used in the results section to validate the numerical simulations.

$$Nu_{Broomley} = 0.62 \left( \frac{Gr Pr}{Ja} \right)^{0.25} \quad (6)$$

$$Nu_{B \& W} = (0.3727 + 0.2738 \left( \frac{1}{D} \right)) \left( \frac{Gr Pr}{Ja} \right)^{0.25} \quad (7)$$

$$\frac{Nu_{Sakurai}}{1 + 2 / Nu_{Sakurai}} = \left[ 0.57 - 0.041 (\log(\bar{D})) + 0.19 (\log(\bar{D}))^2 \right] \left( \frac{Gr Pr}{Ja} \right)^{0.25} \quad (8)$$

Son and Dhir (2007) performed a numerical study of film boiling over a cylinder in three dimensions. They used a Level-set method along with finite-difference discretization of momentum and energy equations to track the vapor-liquid interface. They considered the effects of gravity and cylinder diameter on heat transfer around the cylinder. Moreover, Yuan *et al.* (2007) simulated film boiling over a cylinder using volume-of-fluid (VOF) method based on piecewise linear interface construction (PLIC). They applied special techniques to improve the discontinuous velocity field due to phase change near the interface. To accomplish this, a dual displaced grid with SIMPLE algorithm was used to solve the flow field. Finally, the numerical results were compared with analytical and experimental data.

Nigegowda *et al.* (2014) used combined level-set—VOF method (CLSVOF) along with multidimensional advection algorithm on non-uniform grids to investigate film boiling over a flat surface in two dimensions. They used a finite volume method to discretize the main governing equations. Performance of this hybrid method was examined in terms of mass conservation, application of interfacial force, and mass transfer at interface for different problems. This method was then considered for the simulation of film boiling over flat surface at different surface temperatures.

BeigMohammadi *et al.* (2016) considered, single and multi-nucleus film boil via lattice Boltzmann on a flat horizontal surface in two dimensions. They modeled Rayleigh–Taylor instability by applying an appropriate source term in the Cahn–Hilliard equation. As a result, they showed the effect of Jacob number on Nusselt number, vapor film thickness, and maximum velocity at interface.

## 2. PROBLEM DEFINITION AND GOVERNING EQUATIONS

The prevailing numerical method in the present study is the Front Tracking method. In this method, the interface is specified with a series of definite points. In the course of solution process, these

points are tracked using Lagrangian method. The velocity and pressure fields are solved on a fixed staggered grid. Indeed, this method exhibits the characteristics of both Eulerian and Lagrangian methods. The main advantage of front tracking method is that it can handle curvatures significantly smaller than the size of computational cells.

All the governing equations for film boiling phenomenon are considered in this section. These include conservation of mass, momentum and energy, and the source terms that enter the formulation. Furthermore, the boundary condition for a solid body such as a circular cylinder is explored in detail. In general, conservation equations (including mass, momentum, and energy) are written as follows (for details, please refer to [Esmaeeli and Tryggvason \(2004a\)](#)).

$$\frac{D\rho}{Dt} + \rho \nabla \cdot \mathbf{u} = 0 \quad (9)$$

$$\frac{\partial \rho \mathbf{u}}{\partial t} + \nabla \cdot \rho \mathbf{u} \mathbf{u} = -\nabla P + \rho \mathbf{g} + \nabla \cdot \mu (\nabla \mathbf{u} + \nabla \mathbf{u}^T) + \mathbf{f}_m \quad (10)$$

$$\frac{\partial \rho c T}{\partial t} + \nabla \cdot \rho c \mathbf{u} T = \nabla \cdot k \nabla T + f_e \quad (11)$$

Here, viscous dissipation term in the energy equation is neglected since the velocity gradient is small in the present problem. The above equations are valid in different phases, but the conditions for jump at the interface for the mass and momentum and energy equations are defined as follows:

$$\rho_l (\mathbf{u}_l - \mathbf{u}_f) \cdot \mathbf{n} = \rho_v (\mathbf{u}_v - \mathbf{u}_f) \cdot \mathbf{n} = \dot{m} \quad (12)$$

$$\dot{m} (\mathbf{u}_v - \mathbf{u}_l) = (\tau_v - \tau_l) \cdot \mathbf{n} - (P_v - P_l) \mathbf{l} \cdot \mathbf{n} + \sigma \kappa \mathbf{n} \quad (13)$$

$$\dot{m} h_{fg} = \dot{q} = k_v \left. \frac{\partial T}{\partial n} \right|_v - k_l \left. \frac{\partial T}{\partial n} \right|_e \quad (14)$$

In these equations,  $\mathbf{u}_l$  and  $\mathbf{u}_v$  are fluid velocities in liquid and vapor phases, respectively;  $\mathbf{u}_f$  is the velocity of interface, and  $\dot{m}$  is the vaporization rate at the interface. It is assumed that the temperature at the interface,  $T_f$ , is equal to saturation temperature at the corresponding pressure, i.e.:  $T_f = T_{sat}(P_{sys})$ .

In general, Eqs. (9) - (10) and (12) - (14) should be solved for each phase, and at the interface. Considering the jump condition at the interface, momentum and energy equations take the following forms:

$$\frac{\partial \rho \mathbf{u}}{\partial t} + \nabla \cdot \rho \mathbf{u} \mathbf{u} = -\nabla P + \rho \mathbf{g} + \nabla \cdot \mu (\nabla \mathbf{u} + \nabla \mathbf{u}^T) + \sigma \int \delta(\mathbf{x} - \mathbf{x}_f) \kappa_f \mathbf{n}_f dA_f \quad (15)$$

$$\frac{\partial \rho c T}{\partial t} + \nabla \cdot \rho c \mathbf{u} T = \nabla \cdot k \nabla T - \left[ 1 - (c_v - c_l) \frac{T_{sat}}{h_{fg}} \right] \int \delta(\mathbf{x} - \mathbf{x}_f) \dot{q}_f dA_f \quad (16)$$

Here,  $\delta$  is a two- or three-dimensional delta function which is obtained by successive multiplication of single delta function.  $\mathbf{x}$  is an arbitrary point within the solution domain, and  $\mathbf{x}_f$  is an arbitrary point on the interface (all variables with the subscript  $f$  are related to the interface).

In the past, these equations were solved using second-order projection without taking into account any phase change. If there is no phase change, then Eq. (9) reduces to  $\nabla \cdot \mathbf{u} = 0$  which characterizes incompressible flows. Here, incompressibility is applied to each phase. At the interface, however, compressibility exists due to the change in phase. Even though it is still possible to write Eq. (9) in such a way that it is compatible with the projection method, but the velocity field can be considered as follows:

$$\mathbf{u} = \mathbf{u}_v I + \mathbf{u}_l (1 - I) \quad (17)$$

Here,  $I$  is an indicator functions which takes the value of 1 in vapor phase and the value 0 in liquid phase. Gradient of an indicator function is zero everywhere except at the interface. Therefore, the gradient can be written as a function of the position of the interface as follows:

$$\nabla I = \int \delta(\mathbf{x} - \mathbf{x}_f) \mathbf{n}_f dA_f \quad (18)$$

Taking divergence of Eq. (17) and using Eq. (18) while considering the fact that:

$$\nabla \cdot \mathbf{u}_v = \nabla \cdot \mathbf{u}_l = 0 \quad (19)$$

gives:

$$\nabla \cdot \mathbf{u} = \int \delta(\mathbf{x} - \mathbf{x}_f) (\mathbf{u}_v - \mathbf{u}_l) \cdot \mathbf{n}_f dA_f \quad (20)$$

The difference between the velocities of vapor and liquid phases can be written as a function of the vaporization rate by eliminating  $\mathbf{u}_f$  from Eq. (12).

Knowing that  $\dot{m} = \frac{\dot{q}_f}{h_{fg}}$ , we get:

$$(\mathbf{u}_v - \mathbf{u}_l) \cdot \mathbf{n} = \frac{\dot{q}_f}{h_{fg}} \left( \frac{1}{\rho_v} - \frac{1}{\rho_l} \right) \quad (21)$$

Substituting this equation into Eq. (20), the mass conservation equation can be obtained as follows:

$$\nabla \cdot \mathbf{u} = \frac{1}{h_{fg}} \left( \frac{1}{\rho_v} - \frac{1}{\rho_l} \right) \int \delta(\mathbf{x} - \mathbf{x}_f) \dot{q}_f dA_f \quad (22)$$

In general, it can be declared that the Eqs. (15), (16), and (22) should be solved. These equations are solved using a second-order temporal-spatial

method on a staggered grid, as is detailed below.

In the present paper, simulations are performed in two dimensions. The interface is divided into smaller elements using a set of points. At the beginning of a time step, an indicator function,  $I$ , is specified, with the  $I$  being depended on  $\mathbf{x}_f$ . In order to solve Eq. (18) a Poisson equation is obtained as follows:

$$\nabla^2 I = \nabla \cdot [\delta(\mathbf{x} - \mathbf{x}_f) \mathbf{n}_f dA_f] \quad (23)$$

The right-hand side can be found by obtaining the value of  $\mathbf{n}_f dA_f$  for every element and distribute it on the fixed grid using a Peskin distribution. This equation is solved using a fast Poisson solver (Schumann and Sweet (1976)). Fluid properties including density, viscosity, thermal conductivity, and heat capacity are calculated using the indicator function. In other words,  $\phi^n = \phi_v I^n + \phi_l (1 - I^n)$ , where  $\phi$  can be either of thermophysical or transport properties of the fluid. The heat source term,  $\dot{q}_f$ , is estimated using Eq. (14), and by a first-order discretization:

$$\dot{q}_f = \frac{1}{\Delta} [k_v (T_v - T_{sat}) - k_l (T_{sat} - T_l)] \quad (24)$$

where  $T_l$  and  $T_v$  are the temperatures of liquid and vapor phases near the interface on the liquid and vapor sides, respectively.  $T_{sat}$  is the temperature at interface which is considered to be the saturation temperature of the liquid.  $T_l$  and  $T_v$  are interpolated at locations  $\mathbf{x}_l = \mathbf{x}_f - \Delta \mathbf{n}_j$  and  $\mathbf{x}_v = \mathbf{x}_f + \Delta \mathbf{n}_j$ , respectively. This interpolation is performed at a distance  $\Delta$  in liquid and vapor phases. Numerical studies show that the results of numerical solution are not sensitive to the value of  $\Delta$  as long as  $h \leq \Delta \leq 2h$  (Esmaeeli and Tryggvason (2004a)). In this inequality,  $h$  denotes the size of the computational grid. Once  $\dot{q}_f$  was found, as the final term in Eq. (16), it is distributed on the fixed grid using Peskin distribution.

In order to find the position of the interface, one should integrate the following equation in time:

$$\frac{d\mathbf{x}_f}{dt} = u_n \mathbf{n}_f \quad (25)$$

where  $u_n = \mathbf{u}_f \cdot \mathbf{n}$ . Vertical component of the velocity at interface is obtained using Eqs. (14) and (12):

$$u_n = \frac{1}{2} (\mathbf{u}_v + \mathbf{u}_l) \cdot \mathbf{n} - \frac{\dot{q}_f}{2hfg} \left( \frac{1}{\rho_v} - \frac{1}{\rho_l} \right) \quad (26)$$

As can be seen from Eq. (26), the normal component of the velocity at the interface is composed of two parts. The first part is related to the convection, whereas the second part being related to phase change. Therefore, having the right-hand side of Eq. (25) and integrating it, one can easily find the position of interface at the next time step:

$$\mathbf{x}_f^{n+1} = \mathbf{x}_f^n + \Delta t u_n \mathbf{n}_f \quad (27)$$

Having the position of the interface at the new time step, the indicator function  $I^{n+1}$  is obtained, and the new properties  $\rho^{n+1}, \mu^{n+1}, k^{n+1}, c^{n+1}$  are determined. Moreover, having the position of the interface at the beginning of every time step, the interfacial tension term can be obtained from Eq. (15). The semi-discretized form of the energy equation is as follows:

$$\rho^n c^n \left( \frac{\hat{T}^{n+1} - T^n}{\Delta t} \right) = A^n \quad (28)$$

where  $A$  represents the right-hand side of Eq. (16) which includes convection, diffusion and also source term,  $\dot{q}_f$ . In this equation, the temperature

at next time step is denoted by  $\hat{T}^{n+1}$ .  $T^{n+1}$  should be corrected within and on the boundary of the solid zone, so as to be able to apply temperature boundary condition appropriately on the solid boundary. For this purpose, another indicator function is defined for the solid boundary denoted by  $S$ .  $S$  is zero for the points within the solid boundary and is 1 outside it (Esmaeeli and Tryggvason (2004b)). Therefore:

$$T^{n+1} = T_W (1 - S) + \hat{T}^{n+1} S \quad (29)$$

Similarly, in order to introduce the solid boundary into the momentum equation and apply no slip on the solid boundary, the indicator function  $S$  is used to impose the zero velocity within that zone. Semi-discretized form of the momentum equation is as follows:

$$\frac{\rho^{n+1} \mathbf{u}^{n+1} - \rho^n \mathbf{u}^n}{\Delta t} = -\nabla P + \mathbf{B} \quad (30)$$

In this equation,  $\mathbf{B}$  includes the convection, diffusion, gravity force, and interfacial tension terms. Using the projection method, the above equation is divided into two parts:

$$\frac{\rho^{n+1} \mathbf{u}^{**} - \rho^n \mathbf{u}^n}{\Delta t} = \mathbf{B} \quad (31)$$

$$\frac{\rho^{n+1} \mathbf{u}^{n+1} - \rho^{n+1} \mathbf{u}^{**}}{\Delta t} = -\nabla P \quad (32)$$

In these equations,  $\mathbf{u}^{**}$  is the velocity calculated from Eq. (31), and should be modified to be able to have zero velocity within the solid zone:

$$\mathbf{u}^* = S\mathbf{u}^{**} \quad (33)$$

Next, taking divergence of Eq. (31), the pressure equation is obtained; however, one should replace  $\mathbf{u}^{**}$  with the modified version of that, i.e.  $\mathbf{u}^*$ . This gives:

$$\nabla \cdot \frac{1}{\rho^{n+1}} \nabla P = \frac{\nabla \cdot \mathbf{u}^* - \nabla \cdot \mathbf{u}^{n+1}}{\Delta t} \quad (34)$$

In the above equation, one should use Eq. (22) to obtain  $\nabla \cdot \mathbf{u}^{n+1}$ . The pressure equation is solved using a multigrid solver developed by Adams (1989). Furthermore, in order to evaluate Eq. (32), one should replace  $\nabla P$  by  $S\nabla P$ .

In film boiling over flat surface, a layer of vapor with lower density lies beneath the liquid with higher density in the presence of gravity and interfacial tension. Therefore, formation and release of vapor bubbles into the upper liquid results from Rayleigh – Taylor instability.

Broomley (1950), Hosler and Westwater (1962), and Broomley (1950) were the first to observe the film boiling experimentally. The spacing in the vapor layer where bubbles grow and depart continuously is denoted by  $\lambda_i$  in their study. This spacing can vary as follows:

$$\lambda_c < \lambda_i < \sqrt{3}\lambda_c \quad (35)$$

and  $\lambda_c$  is named as the most critical wavelength of Rayleigh – Taylor instability.  $\lambda_c$  is obtained as follows:

$$\lambda_c = 2\pi \sqrt{\frac{\sigma}{(\rho_l - \rho_v)g}} \quad (36)$$

In wavelengths shorter than  $\lambda_c$ , no instability or bubble growth may happen. Berenson (1961) used a linear stability analysis to show that maximum instability occurs when wavelength is equal to  $\lambda_d$ .

$$\lambda_d = \sqrt{3}\lambda_c \quad (37)$$

where  $\lambda_d$  refers to the most dangerous wavelength. Therefore, in order to have Rayleigh – Taylor instability or bubble growth, the computational domain should be larger than the wavelength  $\lambda_d$ .

However, considering the findings of Lienhard and Wong (1964), for film boiling on a cylinder, the most dangerous wavelength on the cylinder,  $\lambda_{dc}$ , is as follows:

$$\lambda_{dc} = \frac{\lambda_d}{\sqrt{1 + \frac{2}{D^2}}} \quad (38)$$

$$\bar{D} = \frac{D}{L} \quad (39)$$

$$L = \sqrt{\frac{\sigma}{(\rho_l - \rho_v)g}} \quad (40)$$

In these relations,  $D$  is the cylinder diameter and  $L$  is the reference length used for making the parameter dimensionless. Therefore, for cylinders with small and medium diameter (reference to  $L$ ), the most dangerous wavelength on the cylinder,  $\lambda_{dc}$ , is less than the most dangerous wavelength on a flat surface. This is while for the cylinders with large diameters, these two quantities are nearly the same.

In the simulations performed in the present study the length of the computational domain is selected such that it corresponds to the highest rate of instability or growth of bubbles. In other words, in all simulations involving one cylinder, the length of the domain is equal to  $\lambda_d$ .

### 3. RESULTS AND DISCUSSION

#### 3.1 Validation

In order to ensure the reliability of the developed numerical method regardless of the energy equation, a normal single-phase flow over an array of cylinders is simulated. As was mentioned in the previous section, an indicator function,  $S$ , is used to construct the solid boundary. We follow Al-Rawahi and Tryggvason (2002) who used this method to simulate the flow over a large number of long and parallel cylinders by an applied pressure gradient for different solid fractions. Due to large number of parallel cylinders, simulations were performed by selecting a cylinder within a square domain and applying the periodic boundary condition on all boundaries. Solid fraction is equal to the ratio of cross sectional area of the cylinder to the area of the square domain where the cylinder lies:

$$c = \frac{\pi R^2}{L^2} \quad (41)$$

where  $L$  refers to the length of the square domain and is selected as 1, while  $R$  is the radius of the cylinder within domain. For flows at low Reynolds numbers or Stokes flow, Sangani and Acrivos (1982) and Drummond and Tahir (1984) obtained the drag force per unit length of the cylinder analytically:

$$F = 4\pi\mu U \left[ -\frac{1}{2} \ln c - 0.738 + c - 0.887c^2 + 2.038c^3 \right]^{-1} \quad (42)$$

$$F = 8\pi\mu U \left[ \ln\left(\frac{1}{c}\right) - 1.47633597 + \frac{2c - 0.79589781c^2}{1 + 0.48919241c - 1.60486942c^2} \right]^{-1} \quad (43)$$

The results of the proposed relationships for low solid fractions are in complete agreement. In these relations,  $U$  is the average velocity of the flow, and the pressure gradient is related to the drag force via the following relationship:

$$\frac{F}{L^2} = \frac{dP}{dx} \quad (44)$$

$$\tilde{U} = \frac{U\mu}{F} \quad (45)$$

Simulations were performed by assuming  $\frac{dP}{dx} = 1$ ,

$\rho = 1$ , and  $\mu = 1$ , and considering different radii to produce different solid fractions. Considering the assumed values, the resultant Reynolds number will be small, i.e. the flow is in Stokes flow regime. Figure 1 demonstrates the plot of dimensionless average velocity using Eq. (45) versus solid fraction obtained from analytical methods as well as the present work.

As can be seen, the present work is in good agreement with the analytical solutions. The small errors observed at lower solid fractions can be attenuated by using finer grids and utilizing  $S^2$  or  $S^4$ . A  $128 \times 128$  grid is used here.

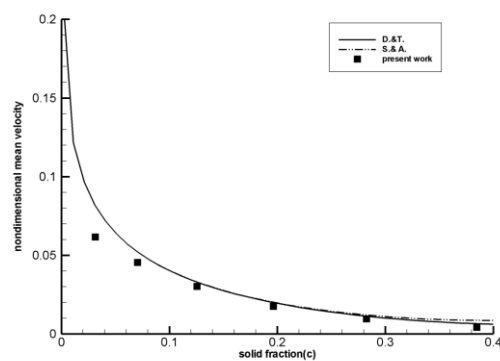


Fig. 1. Plot of dimensionless average velocity versus solid fraction.

### 3.2 Film Boiling Simulation Over a Cylinder

In this section, film boiling phenomenon on a cylinder of given diameter is simulated using the governing equations and front tracking method in two dimensions. First, dimensionless parameters affecting the film boiling are introduced. Then, determination of the Nusselt number is discussed. In order to validate the numerical method, the Nusselt number obtained is compared with experimental data. In order to examine the dependence of results to grid resolution, three different grid resolution are considered. The

average Nusselt number on the cylinder is plotted versus time for three grid resolutions. The effects of important dimensionless parameters on film boiling over a cylinder are investigated and the Nusselt number is plotted against the dimensionless parameters.

In all simulations, zero velocity and constant temperature are assumed on the solid boundary. Of course, temperature is subjected to variations in any simulation. Domain of solution is defined as a rectangle with the boundary conditions as follows: periodic boundary conditions are applied on the right and left boundaries; the lower boundary has the so-called wall boundary condition, and outflow boundary condition is assumed for the upper boundary. Initial conditions are also as follows. A vapor layer surrounds the constant-temperature cylinder. The thickness of this vapor layer is small, so that it can generate vapor bubbles. Indeed, considering the fact that film boiling is a result of Rayleigh-Taylor instability, there should be a small disturbance on the interface between two phases so that the instability grows in time. Radius of this vapor layer is defined as follows:

$$r(y) = r_0 + \varepsilon \cos\left(\frac{2\pi y}{W_x}\right) \quad (45)$$

where  $r_0$  is the average radius of the vapor layer and  $\varepsilon$  is the disturbance amplitude and is taken as 0.001.  $W_x$  is the length of the computational domain. Furthermore, another vapor layer is considered near the upper boundary of the computational domain, so that the generated bubbles can penetrate into the upper vapor layer. In illustrations, the red color marks liquid phase, while the blue color specifies vapor phase. Initial temperatures for two phases are fixed and equal to  $T_{sat}$  (saturation temperature). Other quantities such as velocity and pressure are initialized as zero.

Thermophysical properties of liquid and vapor phases include density, viscosity, thermal conductivity, and specific heat. Other parameters include buoyancy  $((\rho_l - \rho_v)g)$ , excess temperature  $(\Delta T = T_w - T_{sat})$ , interfacial tension  $(\sigma)$ , and latent heat of vaporization  $(h_{fg})$ . As a result, the following dimensionless parameters are obtained:

$$Gr = \frac{\rho_v g (\rho_l - \rho_v) D^3}{\mu_v^2} \quad (46)$$

$$Ja = \frac{c_v \Delta T}{h_{fg}} \quad (47)$$

$$Pr = \frac{\mu_v c_v}{k_v} \quad (48)$$

$$\frac{\rho_l}{\rho_v}, \frac{\mu_l}{\mu_v}, \frac{c_l}{c_v}, \frac{k_l}{k_v} \quad (49)$$

where  $Gr$ ,  $Ja$ , and  $Pr$  refer to Grashof, Jacob, and Prandtl numbers, respectively. The subscript  $v$  characterizes the vapor properties, while  $l$  refers to liquid phase.  $D$  is the cylinder diameter. In all simulations these parameters should be specified. Indeed, these are the main characteristics of every simulation. Regarding with the interfacial tension ( $\sigma$ ), it should be noted that according to the constraint in Rayleigh-Taylor instability, this parameter affects the determination of  $\lambda_d$  which is always equal to the length of the computational domain. In the present simulation, these parameters are taken as the following:

$$Gr = 17.78, Ja = 0.064, Pr = 4.22$$

$$\frac{\rho_l}{\rho_v} = 4.78, \frac{\mu_l}{\mu_v} = 2.58,$$

$$\frac{c_l}{c_v} = 0.546, \frac{k_l}{k_v} = 3.56 \quad (50)$$

Except for Grashof number, the above values are close to the properties of saturated water at 169 bar. A low Grashof number indicates either a fluid with high viscosity or a gravitational acceleration below normal gravitational acceleration, such as that seen in rocket engines. These set of parameters form the basis of our simulations. It is worth to note that, except for Jacob and Grashof numbers, other parameters are always considered to be fixed for all simulations in the present study. Figure 2(a) demonstrates the position of the interface as boiling develops. Figure 2(b) shows the indicator function at the same instants where the interface is shown. It should be noted that, the domain size is  $\lambda_d \times 4\lambda_d$ .

In the present simulation,  $\lambda_d$  is set to 1.3 m. Furthermore, a uniform grid with  $128 \times 512$  grids is used.

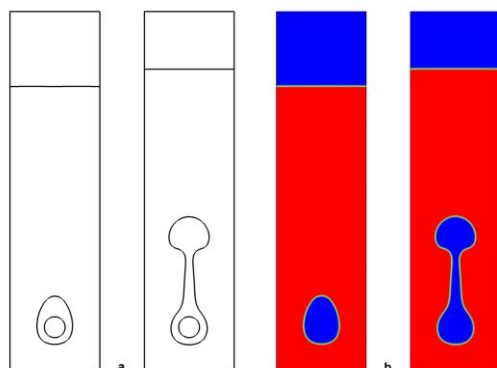


Fig. 2. a- Stages of growth of the interface at 5s (left) and 15 s (right). b- Contours of the indicator function at 5s (left) and 15 s (right).

Figure 2(a) shows the growth of the bubble at two different times. Buoyancy causes the bubble to

move vertically. Upper part of the vapor bubble starts to widen while its lower part becomes thinner. However, after a certain time, due to vaporization and buoyancy force, the thickness of the vapor layer on the lower part of the cylinder becomes constant. Temperature of the cylinder wall prevents further thinning of the lower part of the bubble due to the vaporization of liquid. The upper part of the bubble, however, continues to grow, and develops a mushroom-shape. The bubble tends to be released from the vapor film, provided that the upper part continues to grow. As a result the lower part of the bubble becomes thinner. Several factors control the release of bubble from the vapor film. These include the cylinder temperature which rises the temperature and thereby vaporizes the liquid in the lower part of the bubbles; the growth rate of the upper part of the bubbles; also the interfacial tension which contribute to thinning of the vapor layer.

Figure 2(b) shows contours of the indicator function. This function is one in liquid and zero in vapor and, varies between zero and one as one moves across the interface. The higher the grid resolutions, the lower is the thickness of this zone (the zone where the indicator function changes.) However, considering the fact that the solid body is introduced into the flow using its specific indicator function, the cylinder boundary is not evident in this figure.

Velocity field and temperature distribution at time 15 (s) is shown in Figs. 3(a) and 3(b). The maximum velocity occurs at the center of vapor bubble due to buoyancy force. The temperature in the cylinder is adjusted to 4K and the saturation temperature is 0. It can be seen easily that the vapor phase region temperature is 0, corresponding to Fig. 2.

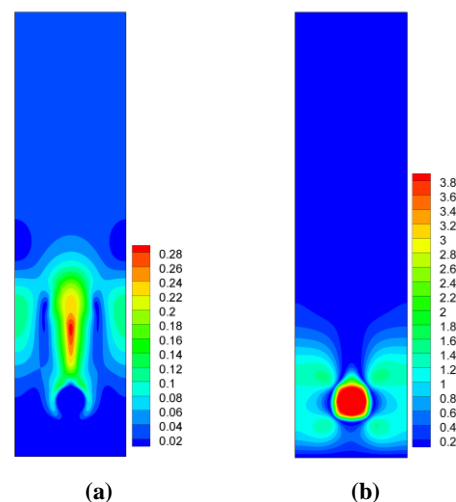


Fig. 3. a-velocity field at 15 s b- temperature contour at 15 s.

The heat transfer rate is important for different industrial applications such as heat exchangers. As such, one should have an appropriate understanding of the heat transfer and its dependence to different

factors such as Grashof and Jacob numbers. For this purpose, the Nusselt number, which is in fact the dimensionless temperature gradient over the object surface, can quantify the heat transfer rate on the cylinder surface. Nusselt number for a cylinder is given by:

$$Nu = \frac{hD}{k} \quad (51)$$

According to the definition of convection heat transfer coefficient:

$$h(T_w - T_{sat}) = -k \frac{\partial T}{\partial n} \quad (52)$$

where  $n$  denotes the direction of the normal to the cylinder surface. Therefore, the Nusselt number becomes:

$$Nu(\theta, t) = -\frac{D}{T_w - T_{sat}} \frac{\partial T}{\partial n} \quad (53)$$

The Nusselt number in the above equation depends on time and position.  $\theta$  is the polar angle defined on the cylinder surface. In order to determine the spatial average Nusselt number, one should integrate the Nusselt number over the perimeter of the cylinder:

$$\langle Nu(t) \rangle = \frac{1}{2\pi} \int_0^{2\pi} Nu(\theta, t) d\theta \quad (54)$$

In order to obtain spatial-temporal average Nusselt number, we have:

$$\langle Nu \rangle = \frac{1}{\Delta t} \int_{t_i}^{t_e} \langle Nu(t) \rangle dt \quad (55)$$

where  $t_i$  is the starting time of pseudo-steady state and  $t_e$  denotes end of simulation. In case the bubbles are released periodically with time,  $\langle Nu(t) \rangle$  will reach a pseudo-steady state after some transition period. But if the bubbles turn into jet, and do not leave the vapor layer, the simulation will end up with steady state, so that changes in Nusselt number will be negligible as time proceeds.

### 3.2.1 Grid Study

In order to ensure independence of the results to grid resolutions, the Nusselt number (i.e. spatial average Nusselt number) is plotted versus time for three different grids ( $64 \times 256$ ,  $128 \times 512$ , and  $256 \times 1024$ ). According to Fig. 4, it is observed that the Nusselt Number for two fine grids are close to one another. Hence, subsequent simulations were performed with a  $128 \times 512$  grid resolution.

As it can be seen from Fig. 4, the Nusselt number begins with rising due to high temperature gradient over the surface. However, as time progresses heat is transferred from the cylinder surface to the vapor layer, and thereby the temperature gradient on the surface is reduced. As a result the Nusselt number decreases. As the vapor bubble continues to grow,

average thickness of the vapor layer on the cylinder surface decreases. This increases the heat flux introduced into the vapor layer, and thereby increasing the vaporization rate. Thus, the temperature gradient near the surface increases thereby increasing the Nusselt number. Since, the created bubble moves upward with a small thickness, and is not separated in this simulation, the Nusselt number converges to a constant value. This is the spatial-temporal average Nusselt number. Here, the Nusselt number is estimated to be  $Nu = 2.47$ .

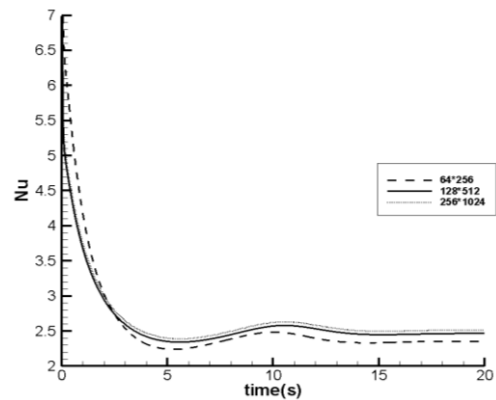


**Fig. 4. Plot of Nusselt number versus time for three different types of grid ( $64 \times 256$ ,  $128 \times 512$ , and  $256 \times 1024$ ).**

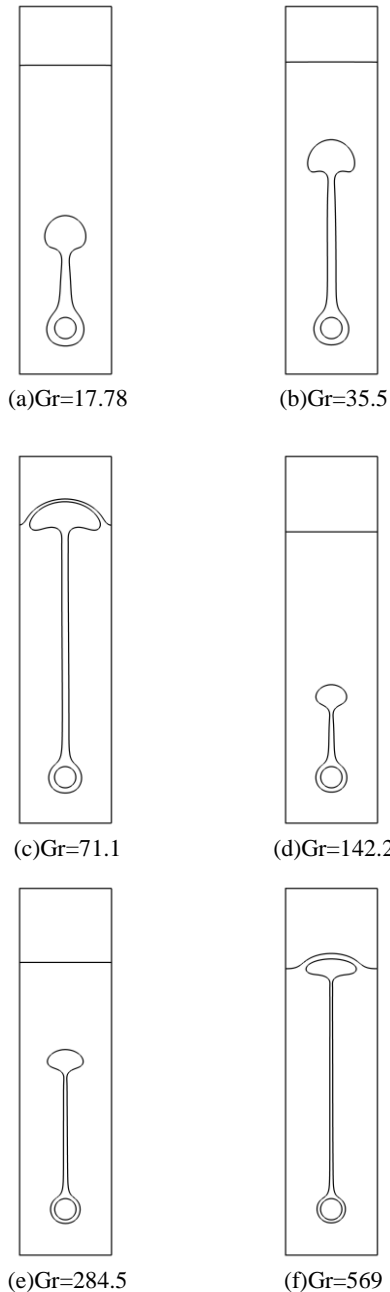
Broomley, Breen and Westwater and Sakurai obtained the following Nusselt numbers, respectively:

$$Nu_{Br} = 3.63 \quad Nu_{BW} = 2.82 \quad Nu_{Sa} = 1.68$$

One of the major causes of the difference between the obtained Nusselt number here and that from the above references is the two-dimensional nature of the simulations in the present study. It is obvious that, in a three-dimensional simulation, a large number of bubbles will grow along the length of the cylinder, while in the two-dimensional simulations, only one vapor bubble is developed either in jet or periodic form.

### 3.3 Effect of Grashof Number on Film Boiling Over a Cylinder

In this section, the effect of Grashof number on the boiling process is demonstrated by keeping the Jacob number and all other parameters constant. Figure 5 illustrates that, the larger the Grashof number, the larger will be the curvature of the generated bubble, and the thinner will be the vapor layer. Here, gravitational acceleration ( $g$ ) is raised in order to increase the Grashof number. Other flow parameters are given by Eq. (50). Furthermore, the most dangerous wavelength,  $\lambda_d$ , is the same for all cases. The shapes of the interface in cases a, b, and c are at time  $t=15$  s. However, in cases d, e, and f, due to high gravitational force and larger velocity of the vapor bubble as it moves upward, the shapes of interface are at time  $t=4$  s.



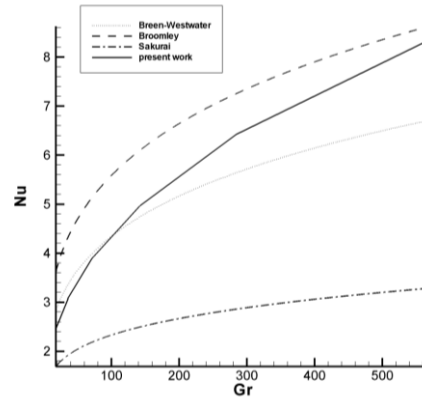
**Fig. 5. Shape of the interface at 15s (cases a, b, and c) and 4 s (cases d, e, and f).**

Figure 6 demonstrates the variation of Nusselt number with respect to the Grashof numbers based on the parameters given in Eq. (50). As can be seen, the Nusselt number increases with increasing the Grashof number accordingly. This behavior has been further investigated in the experiments performed by Broomley, Breen and Westwater and Sakurai. The Nusselt number predicted here shows good agreement with these results, indicating the validity of the present numerical results.

### 3.4 Effect of Jacob Number on Film Boiling Over a Cylinder

We study the effect of wall superheat on the shape of the interface as well as the Nusselt number. This directly affects the Jacob number. Experimental

investigations show that, when Jacob number increases, frequency of bubble generation and vapor layer thickness increases. Also the vapor bubble size increases as well. In some cases, the vapor bubble may leave the surface, and move upward in the form of a vapor jet.



**Fig. 6. Plot of Nusselt number versus Grashof number.**

As can be seen in Fig. 7, the vapor layer thickness increases with increasing the Jacob number. This results in a decrease in Nusselt number as the Jacob number is raised. Figure 8 shows good agreement between the results from the present study and the experimental data obtained by Sakurai.

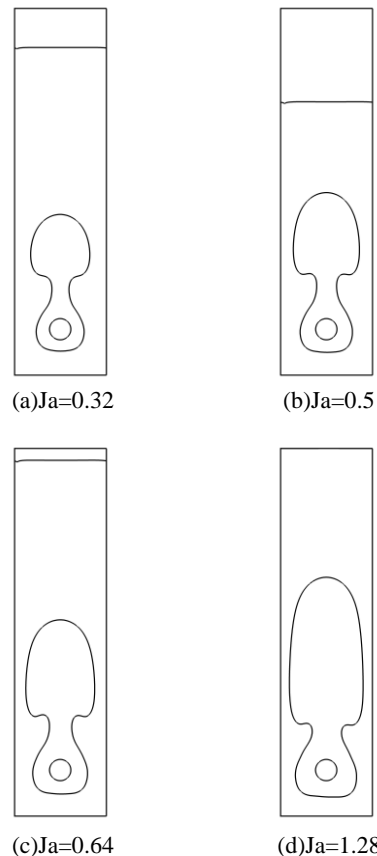


**Fig. 7. Shape of the interface at 15s for different Jacob numbers.**

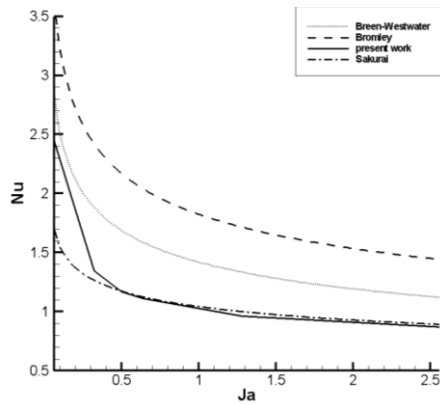


**Fig. 8.** Plot of Nusselt number versus Jacob number.

Another point to note is that, if Jacob number or wall superheat exceeds some certain level, one should consider the effect of radiation in numerical method. Regarding the numerical investigation performed by [Esmaeeli and Tryggvson \(2004c\)](#) in film boiling over a flat surface, the investigated Jacob numbers should be in the range  $0.064 \leq Ja \leq 2.132$  in order to neglect the effect of radiation. On the other hand, if the Jacob number is less than the lower bound, since we are dealing with a very thin vapor layer, grid resolution should be enhanced in the vicinity of the wall and thereby across entire domain. This will increase the associated computational cost considerably. Moreover, with further reduction of the Jacob number, film boiling regime will no longer be established, and transitional boiling regime will dominate.

### 3.5 Effect of Cylinder Spacing on Nusselt Number

Beginning with considering two cylinders, the effects of the spacing between two cylinders, the angle between two cylinders (as shown in figure 9), and also the effect of diameter of the lower cylinder on the heat transfer in the upper cylinder will be investigated. Finally, a large number of cylinders are considered with a few number of rows and different arrangements in order to investigate the Nusselt number for every cylinder.

Two cylinders are considered which are coaxially placed vertically. The Nusselt number in the upper cylinder is determined. The spacing between the two cylinders is changed within 0.35-1.15 m. By the cylinder spacing, we mean surface-to-surface distance. Diameter of every cylinder is fixed at 0.3 m. Boundary conditions are as before. Other flow parameters, including Grashof number, Jacob number, and Prandtl number as well as thermophysical properties are the same as those evaluated in Eq. (50). Furthermore, a vapor layer is also considered close to the upper boundary where the bubbles can penetrate into this layer.

Figure 10 presents film boiling over two coaxial cylinders along vertical direction at a surface-to-surface distance 0.55 m. It can be seen that, as the vapor bubble grows from the lower cylinder and

gets close to the upper cylinder, vapor bubble of the lower cylinder surrounds the upper cylinder. Finally, it reaches to a point where the upper cylinder is covered by only vapor.

Figure 11-a shows the Nusselt number versus time for the upper and lower cylinders. As the vapor bubble of the lower cylinder moves and hits the upper cylinder, the Nusselt number increases, due to the flow disturbances created around the upper cylinder. The Nusselt number for the lower cylinder is equal to the Nusselt number of a single-cylinder when film boiling occurs (investigated in the previous section). Therefore, it can be concluded that, the Nusselt number on the lower cylinder will not be affected by the upper cylinder. This is while the Nusselt number on the upper cylinder is affected by the lower cylinder. This is trivial, because as the vapor bubbles collide to one another, flow disturbances increase, thereby enhancing conventional effects. Since vapor is always produced in boiling regime, it passes through the upper cylinder, and is guided towards the upper vapor layer. Therefore, the Nusselt number reaches a steady state after some transition period.

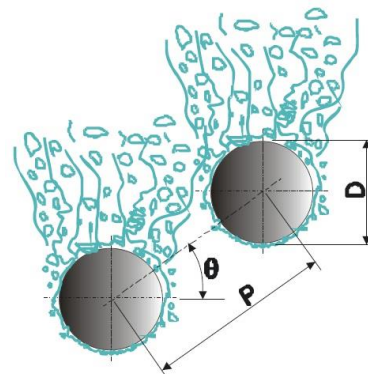


**Fig. 9.** definition of spacing, angle and diameter graphically [Kang \(2015b\)](#).

In Fig. 11(b), Nusselt number is plotted versus time for four different spacing. As can be seen, the Nusselt number is maximum (14.84) when the cylinder spacing is 0.55 m. Minimum Nusselt number (13.99) was obtained when the spacing is 1.15 m. It is observed that, a change in the vertical distance between the two cylinders may not significantly affect Nusselt number. Nevertheless, even this very small increase in Nusselt number at the spacing 0.55 m, can be important in many applications.

### 3.6 Effect of the Orientation Angle Between Two Cylinders on Nusselt Number

Here, the effect of the angle between two cylinders on the Nusselt number is investigated. All the flow conditions are the same as those in the previous section. The orientation angle is defined as the angle between a horizontal line and the line connecting centers of the two cylinders. The angle is changed from  $0^\circ$  to  $90^\circ$  with  $15^\circ$  increments. The cylinder spacing is considered to be constant and equal to 0.55 m. Considering the position of two cylinders within the computational domain, the

length of the domain has been doubled at relatively small angles, while its height is not changed.

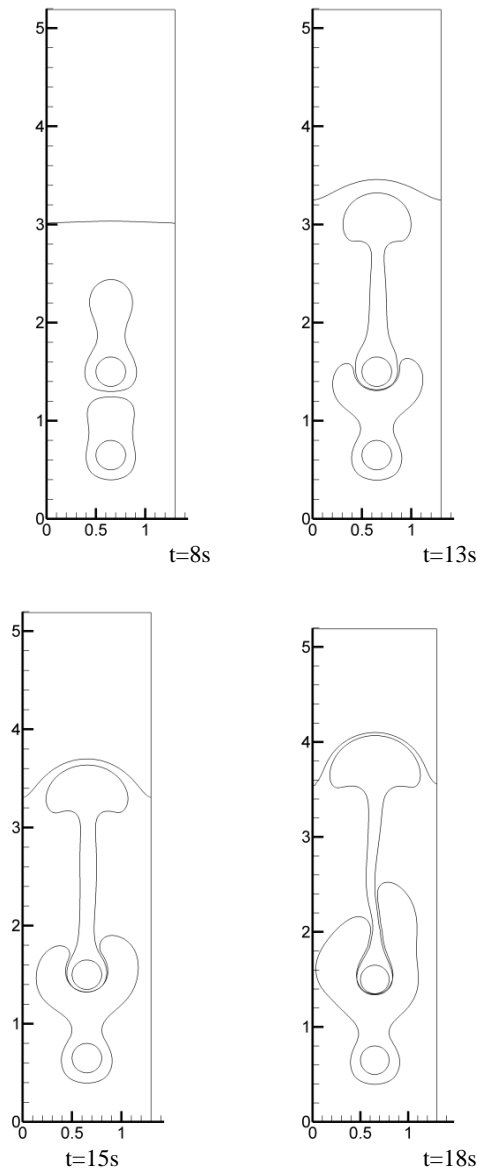


**Fig. 10.** Different stages of bubble growth at various times.

The higher the angle, the more will be the engagement of the upper cylinder with the vapor bubbles rising from the lower cylinder, thereby increasing the Nusselt number. Here again the change in the Nusselt number for the lower cylinder is similar to that of a single-cylinder in previous sections. As can be seen in Fig. 12, the value of Nusselt number is maximum when the angle is  $90^\circ$ , i.e. when the cylinders are coaxial in the vertical direction. This is because the vapor bubbles moving from the lower cylinder are fully engaged with the upper cylinder.

As is evident, when the angle between the cylinders is  $15^\circ$ ,  $75^\circ$ , and  $90^\circ$ , the Nusselt numbers are 2.82, 4.55, and 14.84, respectively. This shows that the arrangement of two cylinders is very important in

terms of the Nusselt number developed on the upper cylinder. The higher the angle, the higher is the Nusselt number. This increase is very large at relatively large angles, as compared to small angles. For instance, corresponding Nusselt number for  $15^\circ$  and  $30^\circ$  are 2.82 and 2.92, respectively; while the corresponding Nusselt numbers for  $60^\circ$  and  $75^\circ$  are 3.8 and 4.55, respectively. This increase will be even larger at angles close to  $90^\circ$ , so that the Nusselt number at  $90^\circ$  reaches 14.84.

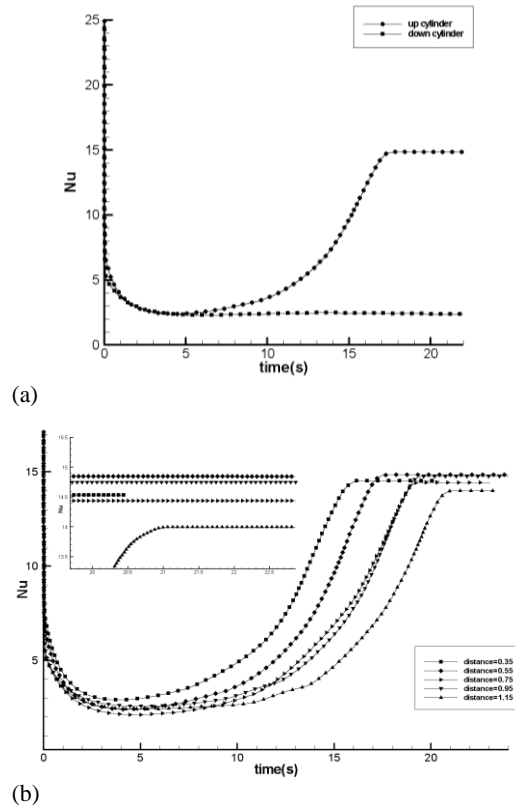


**Fig. 11.** a- Plot of Nusselt number versus time for the upper and lower cylinders. b- Plot of Nusselt number versus time for the upper cylinder at different distances to the lower cylinder.

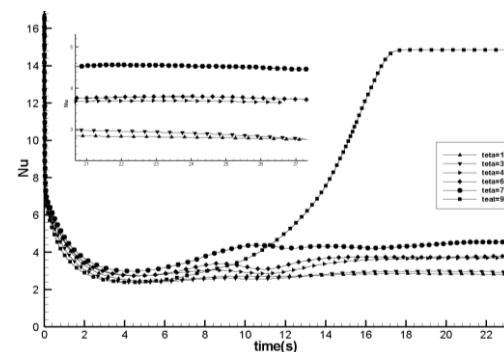


**Fig. 12.** Plot of Nusselt number on the upper cylinder versus time at different angles to the lower cylinder.

### 3.7 Effect of Diameter of the Lower Cylinder on Nusselt Number

Changes in Nusselt number on the upper cylinder

are investigated by changing the diameter of the lower cylinder. Since the upper cylinder is influenced by the lower cylinder, the diameter of lower cylinder is changed. Accordingly, the diameter of the upper cylinder was fixed at 0.3 m. Center-to-center distance of two cylinders is 1 m, and the angle between them is 90°. As the bubbles grow and rise, the vapor bubbles generated from the lower cylinder surround the upper cylinder, and results in enhanced convection and increase in Nusselt number. Figure 13 shows the Nusselt number as a function of time for different diameters.

It can be seen that, the Nusselt number is maximum (19.2) for a diameter 0.6 m. As the diameter increases from 0.2 m to 0.6 m, the Nusselt number increases accordingly. With increasing the diameter beyond 0.6 m, the Nusselt number decreases. Another point to note is that, maximum value of the Nusselt number in this case is higher than the Nusselt numbers found in the previous two sections. That is, the Nusselt number can be further enhanced by changing the diameter of the cylinders.

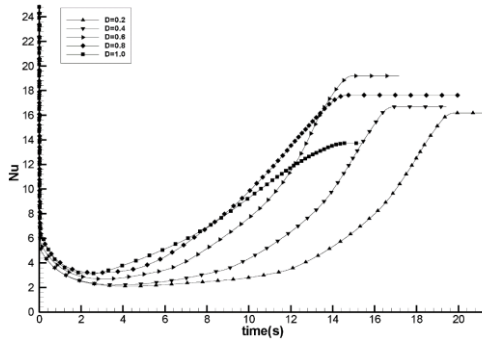


**Fig. 13. Plot of Nusselt number on the upper cylinder versus time for different diameters of the lower cylinder.**

### 3.8 Effect of the Arrangement and Number of Rows of Cylinders

In three previous sections, we studied film boiling over two cylinders by considering different cylinder spacing, angles and diameters of the lower cylinder. In general, it was observed that, if the upper cylinder is influenced more by the vapor bubbles from the lower cylinder, the disturbances are enhanced. As a result, the heat transfer coefficient and the Nusselt number enhance as well. Considering the fact that in most industrial applications, film boiling occurs on a large number of pipes or cylinders, it seems necessary to simulate this phenomenon on more complex geometries composed of a large number of cylinders. Such simulations can help in finding the heat transfer coefficient using the Nusselt number on every pipe. This may end up with optimal design of pipe arrangement. Here, two arrangements of the cylinders, namely regular and staggered, are considered. Number of cylinders in each row is considered to be 5. In each arrangement, the effect of number of rows on the Nusselt number of the upper cylinders are investigated. The Nusselt

numbers are plotted versus time for each of the cylinders in the upper row. Finally, according to Nusselt number obtained for every cylinder in the upper row, a comparison is made between these cylinder arrangements.

Cylinder spacing, is 0.9 m in both horizontal and vertical directions. Diameter of every cylinder is also fixed at 0.3 m.

Figures 14 demonstrate the growth and rise of bubbles at different times for 4 rows of cylinders. As can be seen, the vapor bubbles grow from the lower cylinders and once passed through the upper cylinders, surround them. Furthermore, the grown bubbles further rise towards the vapor layer on top of the computational domain.

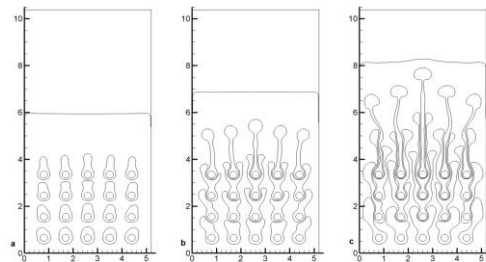


**Fig. 14. a- Shape of interface at 5 s. b- Shape of interface at 10 s. c- Shape of interface at 15 s.**

It should be pointed out that it is probable that the interfaces developing from the lower and upper cylinders merge when they grow in time which is not considered in the present study.

Next, the values of Nusselt numbers over every cylinder are investigated. As was seen in previous sections, the Nusselt number over the lower cylinders is independent of the upper cylinders. This is due to the fact that the lower cylinders are not affected by the disturbances created by themselves. The Nusselt number on these cylinders correspond to the Nusselt number on a single cylinder. Therefore the Nusselt number over the lower cylinders is not reported here.

The cylinders are numbered in order to plot the Nusselt number against time for the cylinders in the second, third, and fourth rows. Thus, the cylinders in the second, third, and fourth rows were numbered as 6 to 10, 11 to 15, and 16 to 20, respectively. Figures 15 show Nusselt number as a function of time for two, three, and four rows of cylinders in the regular arrangement. Note that, in every figure, only the Nusselt numbers of the cylinders in the upper row are plotted.

With reference to Fig. 15(a), when two rows of cylinders are used in a regular arrangement, corresponding Nusselt numbers for cylinders 6 and 10 are nearly the same, and is equal to 6.4. However, for cylinders located in the central section, i.e. cylinders 7, 8, and 9, the Nusselt number is higher due to higher engagement with the vapor bubbles. The Nusselt number on cylinder 9 is 7.78. However, when three rows of cylinders are incorporated into the arrangement, (Fig. 15(b)), the Nusselt number for the cylinders in the third row is

enhanced compared to the second row. In fact, the cylinders in the first and second rows contribute largely to the enhancement of the Nusselt number of the cylinders in the third row. The increase in the Nusselt number of the cylinders in the second rows has been solely depended on the cylinders in the first row. It is observed that, the Nusselt numbers on almost all cylinders in the third row are close to one another, and the Nusselt number on cylinder 15 is around 8.13. When simulation is performed with four rows of cylinders (Fig. 15(c)), it is observed that the Nusselt number falls somehow below those of the cylinders in the third row. The maximum Nusselt number (7.62) is recognized on cylinder 16. This situation can be explained by the fact that, the flow disturbances developed with the growth of the vapor bubbles generated by the cylinders in the first and second rows has failed to reach the cylinders in the fourth row. They rather enhanced the Nusselt number on the cylinders in the third row. The increase in Nusselt number on the cylinders in the fourth row is mainly a result of the bubbles risen from the third row. In fact, it can be concluded that the effect of flow convection, which is developed from the growth and movement of the vapor bubbles of the lower cylinders, affects the cylinders in the third row while its effects on the cylinders in upper row weakens.

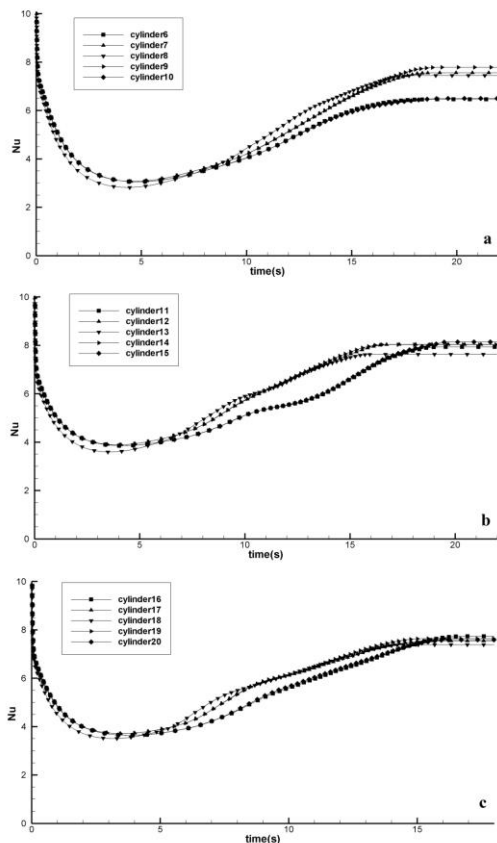


**Fig. 15. a-** Plot of Nusselt number versus time for simple arrangement with two rows of cylinders. **b-** Plot of Nusselt number versus time for simple arrangement with three rows of cylinders. **c-** Plot of Nusselt number versus time for simple arrangement with four rows of cylinders

In the staggered arrangement, every cylinder in the upper row is placed such that it locates between cylinder pairs in the lower row. The vertical and horizontal center-to-center distances between all adjacent cylinders is again equal to 0.9 m. All cylinders have the same diameter (0.3 m). Dimensions of the computational domain are set such that adequate space is available for liquid phase change around the cylinders. The entire flow simulation is similar to that in regular arrangement. In addition, cylinder numbering is performed the same way as the regular case.

Figures 16 show the Nusselt number versus time for staggered arrangement with different numbers of rows of cylinders. The variations of Nusselt number with time is as shown in Fig. 16(a) when two rows of cylinders are used. It can be seen that the Nusselt number on cylinders 6 to 9 are close to each other. This is while cylinder 10 exhibits lower Nusselt number (3.68) because of lower flow disturbance. However, the value of Nusselt number on cylinder 9 is maximum (5.86). It is evident, that the Nusselt number on the cylinders in the second row in regular arrangement is higher than those of the staggered arrangement.

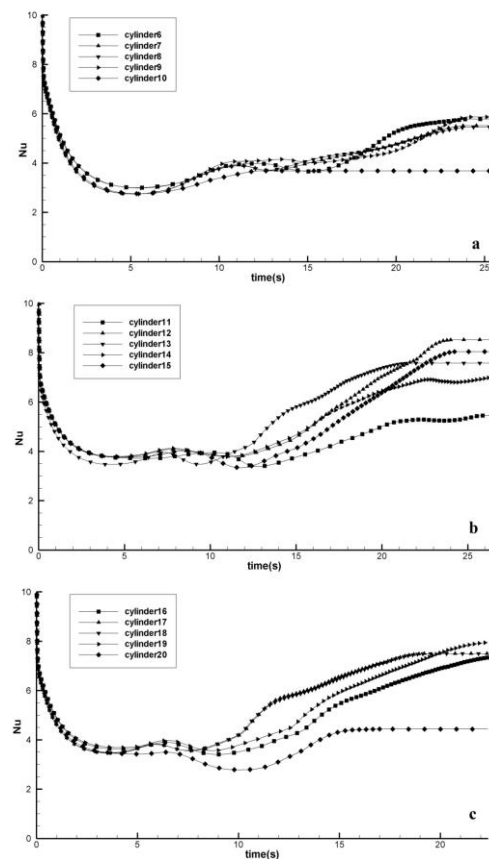


**Fig. 16. a-**Plot of Nusselt number versus time for the displaced(staggered) arrangement with two rows of cylinders. **b-** Plot of Nusselt number versus time for the displaced arrangement with three rows of cylinders. **c-**Plot of Nusselt number versus time for the displaced arrangement with four rows of cylinders.

In Fig. 16(a), it is seen that the Nusselt number of

the cylinders in the third row are considerably different from each other. These values on the cylinders 11, 12, 13, 14, and 15 are 5.2, 8.52, 7.58, 7, and 8.04, respectively. This is while the corresponding values in the regular arrangement were very close to each other. It can be inferred that, in the staggered arrangement, the complexity of the flow geometry is such that and the flow disturbance and the effect of vapor bubbles rising from the lower cylinders affect the cylinders in the third row nonuniformly. As a result, the Nusselt number for the cylinders in this row are somehow different from each other.

When four rows of cylinders are used in staggered arrangement, the Nusselt number on the cylinders 16 to 19 at the end of simulation are very close to each other (Fig 16(c)). The Nusselt number on cylinders 16, 17, 18, and 19 are 7.34, 7.49, 7.49, and 7.94 respectively. Comparing Figs. 16(c) and 15(c), it can be observed that the Nusselt numbers of the cylinders on the fourth row in the staggered arrangement are close to each other, and on average, these are relatively higher than the Nusselt numbers of the cylinders in the fourth row in regular arrangement. It can be inferred that, the flow disturbance resulted from the growth of the vapor bubbles has larger impact on the cylinders in the fourth row in staggered arrangement, compared to regular arrangement.

#### 4. CONCLUSION

Film boiling has numerous applications in different industries. Numerical studies are essentially required to better understand this phenomenon. So far most of the numerical studies performed on this phenomenon has been performed on simple geometries, (either in two or three dimensions). Investigations of film boiling on more complex geometries have been limited to analytical or experimental works. Analytical studies are based on numerous simplifications, while experimental investigations are relatively expensive. The present work deals with numerical simulation of film boiling, using front tracking method, over a large number of cylinders in two dimensions. The heat transfer in xxxxxxxx number was studied next. The Nusselt number is strongly depended on the relative orientation angle. It becomes maximum at an orientation angle  $90^\circ$ . The effect of diameter of the lower cylinder on the Nusselt number of the upper cylinder was also investigated. The overall result was that, the larger the level of flow disturbance, the higher will be the Nusselt number. The level of disturbance is indeed a functions of the engagement of vapor bubbles generated from the lower cylinder with the upper cylinder. As a result, a larger cylinder imposes larger disturbances which in turns enhances the Nusselt number on the upper cylinder. The number of cylinders was increased in order to investigate the effect of the adjacent cylinders on the overall Nusselt number. Two arrangements (regular and staggered) were considered, and the cylinders were arranged in different numbers of rows. The effect of the number

of rows on the Nusselt number of the cylinders in the upper row was investigated for every arrangement, and a comparison was made between the two arrangements. It was found that the Nusselt numbers on the upper cylinders are more nonuniform in staggered arrangement compared to the regular arrangement. Also the overall Nusselt number was higher for the upper row in staggered arrangement compared to regular arrangement. In fact, the results of this section can be used for design, manufacturing and optimization of the heat exchangers wherein film boiling regime exist

#### REFERENCES

- Adams, J. (1989). MUDPACK: multigrid FORTRAN software for the efficient solution of linear elliptic partial differential equations. *Applied Mathematics and Computation* 34, 113-146.
- Al-Rawahi, N. and G. Tryggvason (2002). Numerical simulation of a dendritic solidification with convection: two-dimensional geometry. *Journal of Computational Physics* 180(2), 471-496.
- Begmohammadi, A., M. H. Rahimi, M. Farhadzadeh and M. Abbasi Hatani (2016). Numerical simulation of single-and multi-mod film boiling ussing lattice Boltzmann method, *computers and Mathematics with Applications* 71(9), 1861-1874.
- Berenson, P.J. (1961). Film-boiling heat transfer from a horizontal surface. *ASME Trans, Journal of Heat Transfer* 83(3), 351-356.
- Breen, B. P. and J. W. Westwater (1962). Effect of diameter of horizontal tubes on film boiling heat transfer, *Chem.Eng.Progr.*, 58,67-72
- Broomley, L. A. (1950). Heat transfer in stable film boiling, *Chemical Engineering* 46, 221-227.
- Drummond, J. E. and M. I. Tahir (1984). Laminar viscous flow through regular arrays of parallel solid cylinder. *Int. J. Multiphase Flow* ?
- Esmaeeli, A. and G. Tryggvason (2004a). A front tracking method for computations of boiling in complex geometries. *International Journal of Multiphase Flow* 30, 1037-1050.
- Esmaeeli, A. and G. Tryggvason (2004b). Computations of film boiling. Part I: Numerical method. *International Journal of Multiphase Flow*. 30, 1037-1050.
- Esmaeeli, A. and G. Tryggvason (2004c). Computations of film boiling. Part II: multi-mode film boiling. *International Journal of Heat and Mass Transfer* 47, 5463-5476
- Hahne, E. and J. Muller (1983). Boiling on a finned tube and a finned tube bundle. *International Journal of Heat Mass Transfer*. 26, 849-859.
- Hosler, E. R. and J. W. Westwater (1962). Film boiling on horizontal plate. *Journal of the American Rocket Society* 32(4), 553-558.

- Kang, M. G. (2005). Local Pool Boiling Coefficients on Horizontal Tubes, *Journal of Mechanical Science and Technology*, 19(3), 860–869
- Kang, M. G. (2015a). Pool boiling heat transfer on tandem tubes in vertical alignment. *International Journal of Heat and Mass Transfer* 87, 138–144.
- Kang, M. G. (2015b). Effects of elevation angle on pool boiling heat transfer of tandem tubes. *International Journal of Heat and Mass Transfer* 85, 918–923
- Klimenko, V. V. (1961). Film boiling heat transfer from a horizontal surface, *Journal of Heat Transfer* 83, 351–356.
- Lienhard, J. H. and P. T. Y. Wong (1964). The dominant unstable Wavelength and minimum heat flux during film boiling on a horizontal cylinder. *Journal of Heat Transfer*. 86(2), 220-225.
- Liu, Z. H. and Y. H. Qiu (2002a). Enhanced boiling heat transfer in restricted spaces of a compact tube bundle with enhanced tubes. *Applied Thermal Engineering* 22, 1931–1941
- Liu, Z. H. and Y. H. Qiu (2002b). Boiling heat transfer of water on smooth tubes in a compact staggered tube bundle. *Applied Thermal Engineering* 24, 1431–1441.
- Nigegowda, B.M. and B. Premachandran (2014). A couple level set and volume of fluid method with multi-directional advection algorithms for two-phase flows with and without phase change. *Heat and Mass Transfer* 79, 532-550.
- Saini, J. S. and H. K. Varma (1995). Boiling heat transfer in small horizontal tube bundles at low cross-flow velocities. *International Journal of Heat Mass Transfer*. 38, 599–605.
- Sakurai, A. and M. Shiotsu (1990a). A general correlation for pool film boiling heat transfer from a horizontal cylinder to subcooled liquid: part1-A Theoretical pool film boiling heat transfer model including radiation contributions and its analytical solutions. *Journal of Heat Transfer* 12(2), 430-440.
- Sakurai, A. and M. Shiotsu (1990b). A general correlation for pool film boiling heat transfer from a horizontal cylinder to subcooled liquid: part2- Experimental data for various liquids and its correlation. *Journal of Heat Transfer* 112(2), 441-450.
- Sangani, A. S. and A. Acrivos (1982). Slow flow past periodic arrays of cylinder with application to heat transfer. *International Journal of Multiphase Flow* 8(3), 193-206.
- Schumann, U. and R. Sweet (1976). A direct method for the solution of poisson's equation with boundary condition on a staggered grid of arbitrary size. *Journal of computational Physics* 20, 171-182.
- Son, G. and V. Dhir (2007). Three-dimensional simulation of saturated film boiling on a horizontal cylinder. *Heat and Mass Transfer* 51(5–6), 1156-1167.
- Swain, A. and M. D. Kumar (2014). A review on saturated boiling of liquids on tube bundles, *Heat Mass Transfer* 50, 617–637
- Yuan, M.H. and Y.H. Yang (2007). Numerical simulation of film boiling on a spher with a volume of fluid interface tracking method, *Heat and Mass Transfer* 51(7–8), 1646-1657.
- Zuber, N. (1963). Nucleat boiling: The region of isolated bubbles and the simi-larity with natural convection. *International Journal of Heat and Mass Transfer*. 6(1), 53-60.